

Edge microstability of NSTX plasmas without and with lithium-coated plasma-facing components

This content has been downloaded from IOPscience. Please scroll down to see the full text.

2013 Nucl. Fusion 53 113016

(<http://iopscience.iop.org/0029-5515/53/11/113016>)

View [the table of contents for this issue](#), or go to the [journal homepage](#) for more

Download details:

IP Address: 198.35.1.100

This content was downloaded on 27/09/2013 at 15:22

Please note that [terms and conditions apply](#).

Edge microstability of NSTX plasmas without and with lithium-coated plasma-facing components

J.M. Canik¹, W. Guttenfelder², R. Maingi², T.H. Osborne³,
S. Kubota⁴, Y. Ren², R.E. Bell², H.W. Kugel², B.P. LeBlanc²
and V.A. Souhkanovskii⁵

¹ Oak Ridge National Laboratory, Oak Ridge, TN 37831, USA

² Princeton Plasma Physics Laboratory, Princeton University, Princeton, NJ 08543, USA

³ General Atomics, San Diego, CA 92186, USA

⁴ Department of Physics and Astronomy, University of California-Los Angeles, Los Angeles, CA 90095, USA

⁵ Lawrence Livermore National Laboratory, Livermore, CA 94551, USA

E-mail: canikjm@ornl.gov

Received 31 December 2012, accepted for publication 2 September 2013

Published 27 September 2013

Online at stacks.iop.org/NF/53/113016

Abstract

The pedestal structure in NSTX is strongly affected by lithium coatings applied to the PFCs. In discharges with lithium, the density pedestal widens, and the electron temperature (T_e) gradient increases inside a radius of $\psi_N \sim 0.95$, but is unchanged for $\psi_N > 0.95$. The inferred effective electron thermal (χ_e^{eff}) and particle (D_e^{eff}) profiles reflect the profile changes: χ_e^{eff} is slightly increased in the near-separatrix region, and is reduced in the region $\psi_N < 0.95$ in the with-lithium case. The D_e^{eff} profile shows a broadening of the region with low diffusivity with lithium, while the minimum value within the steep-gradient region is comparable in the two cases. The linear microstability properties of the edge plasma without and with lithium have been analysed. At the pedestal top microtearing modes are unstable without lithium. These are stabilized by the stronger density gradient with lithium, becoming TEM-like with growth rates reduced and comparable to $E \times B$ shearing rates. In the region $\psi_N > 0.95$, both the pre- and with-lithium cases are calculated to be unstable to ETG modes, with higher growth rates with lithium. Both cases are also found to lie near the onset for kinetic ballooning modes, but in the second-stable region where growth rates decrease with increasing pressure gradient.

(Some figures may appear in colour only in the online journal)

1. Introduction

The application of lithium coatings to the plasma-facing components (PFCs) of the National Spherical Torus Experiment (NSTX) has been shown to dramatically alter the plasma behaviour, leading to a reduction in divertor particle recycling [1, 2], increased energy confinement [3], and at high lithium levels the complete elimination of edge-localized modes (ELMs) [4]. The plasma edge in particular shows a marked change with lithium coatings applied, with a widening of the pressure pedestal observed [5] that leads to an overall increase in the pedestal-top pressure, contributing to the observed improvement in energy confinement. While the improvements in plasma performance are potentially advantageous for future device, the physics underlying the observed changes has not been established, making

extrapolation uncertain. Here we present an exploration of possible mechanisms involved, through calculations of the linear microstability of NSTX discharges without and with lithium coatings, motivated by interpretive 2D plasma/neutral modelling of the edge transport.

1.1. Summary of 2D modelling results

2D modelling of pre-lithium and with-lithium discharges has been performed using the SOLPS suite of codes [6], which solves a set of coupled fluid plasma and kinetic neutral transport equations. The modelling is iterative, with the ‘anomalous’ cross-field transport coefficients adjusted until agreement is obtained between the measured and modelled midplane density and temperature profiles (divertor heat flux and D_α measurements also constrain the modelling). The

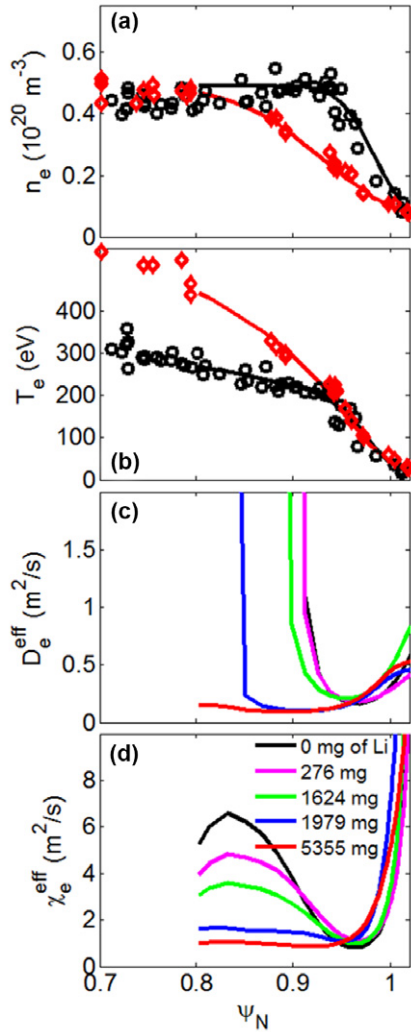


Figure 1. Profiles of (a) n_e , (b) T_e , without (black) and with 5355 mg of lithium (red), and (c) D_e^{eff} and (d) χ_e^{eff} as the amount of lithium is varied.

power flowing from the core into the edge is input as a boundary condition; this is taken to be equal to $P_{\text{NBI}} + P_{\text{OHM}} - P_{\text{RAD}} - dW/dt$, where P_{NBI} and P_{OHM} are the input power from neutral beam injection and ohmic heating, respectively, P_{RAD} is the power radiated in the core plasma, and W is the plasma stored energy. The sources due to neutral recycling are calculated self-consistently. This technique yields ‘effective’ cross-field diffusivities (no attempt is made to discern any convective particle transport), along with the particle recycling coefficient R at the PFC surfaces [7].

A summary of the 2D modelling results for plasmas without and with lithium-coated PFCs is shown in figure 1 (a comprehensive presentation of the modelling approach and results can be found in [8]). The modelling indicates that the application of lithium reduces R from ~ 0.98 to 0.9 [7]. The modelled and measured pedestal profiles (figure 1) show that, with lithium coatings, the electron density (n_e) gradient within the pedestal is reduced by $\sim 50\%$, which is consistent with the reduction in particle source with lithium [8]. The width of the n_e pedestal increases, however, so that the pedestal-top n_e is comparable in the two cases. The electron temperature (T_e)

profile is similar pre- and with-lithium in the region $\psi_N > 0.95$, while the T_e gradient is stronger inside this radius for the with-lithium case. The inferred effective electron thermal (χ_e^{eff}) and particle (D_e^{eff}) profiles reflect these profile changes: χ_e^{eff} is modestly increased outside $\psi_N \sim 0.95$, and is reduced in the region $\psi_N < 0.95$ as the amount of lithium increases. The D_e^{eff} profile shows a broadening of the region with low diffusivity with lithium, while the minimum value within the steep-gradient region is comparable in the various cases. These changes reflect the widening of the pressure pedestal observed with lithium. Electron profiles are emphasized in the present work, since both the ELM stabilization and confinement improvement observed with lithium are attributed to changes in the electron profiles (i.e. the ion pedestal pressure is little changed with lithium [9], and the ion heat transport is modestly increased in contrast to the strong reduction observed with in the electron channel [1, 10]). Changes to the measured ion profiles can be found in [8].

The 2D modelling highlights two edge regions with differing behaviour as lithium is applied. In the far edge outside $\psi_N \sim 0.95$, the T_e profile is approximately unchanged by the application of lithium. The near-constancy of the T_e gradient is observed over a wide range of lithium deposition amounts [8], and in spite of the strong changes in the n_e profile that occur with lithium. This facet of the edge profiles is important to the changes in ELM behaviour observed with lithium: since T_e is unchanged while the n_e profile is reduced, the pressure gradient and bootstrap current in this region is reduced. Stability calculations with the ELITE code [11] have shown that this reduces the drive of the peeling component of peeling–ballooning stability [5], resulting in increased stability with lithium, consistent with the experimental trends of ELM behaviour [5]. Further calculations have also shown that the experimental ELM behaviour across the entire range of lithium deposition amounts is consistent with peeling–ballooning stability (i.e. ELM cases are near the stability boundary, while ELM-free cases are farther into the stable region), and correlates to the modification of the density profile caused by lithium [9].

In the region inside a radius of $\psi_N \sim 0.95$, the effective transport coefficients are reduced as lithium is applied. The electron thermal diffusivity shows a continuous reduction in this region as more lithium is deposited, to the point that a transport barrier is difficult to make out in the maximum lithium case. The particle diffusivity, on the other hand, shows a broadening of the barrier region as lithium is increased, reflecting the measured widening of the n_e pedestal [9].

Turbulence measurements have also been made in these two regions [8]. In the edge region, reflectometry indicates a strong reduction in low- k fluctuations, suggesting a change in the underlying nature of the turbulence. At the pedestal top, high- k microwave scattering measurements show a reduction in fluctuation levels at electrons scales, consistent with the inferred reduced transport.

1.2. Microstability analysis with GS2

The linear microstability properties of these edge plasmas have been analysed using the initial value gyrokinetic code GS2 [12]. The purpose of this study is to explore the physics

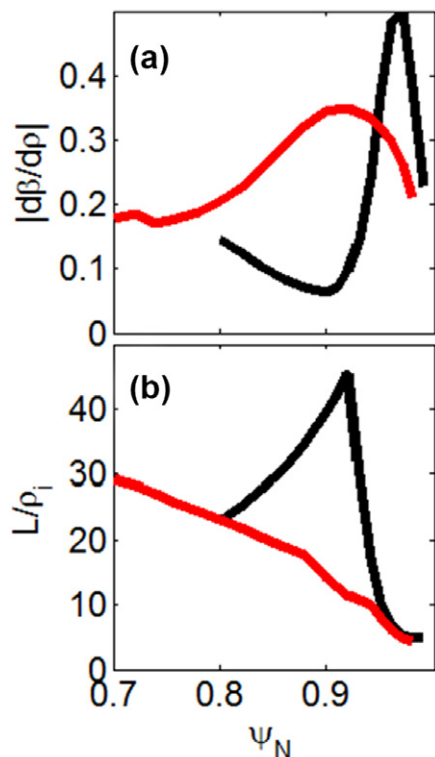


Figure 2. Profiles of (a) pressure gradient, (b) ratio of gradient scale length to ion gyroradius without (black) and with (red) lithium.

behind the transport changes observed in the two regions highlighted by 2D modelling, i.e. to understand why the T_e gradient is fixed at the edge, and why transport is reduced inside $\psi_N \sim 0.95$. Two types of instabilities are of special interest: kinetic ballooning modes (KBM), which have gained interest in the community recently as possibly limiting the pedestal pressure gradient between ELMs [13], and electron temperature gradient modes (ETG), which may play a role in the observed stiffness of the T_e profile for $\psi_N > 0.95$ [8].

Radial profiles of the normalized pressure gradient (shown in terms of $\beta = 2\mu_0 p/B_0^2$) are shown in figure 2, as well as the ratio of the minimum gradient scale length L to the ion gyroradius ρ_i . At the pedestal top, where the pressure gradient (panel (a)) is relatively small compared to its peak value, $L/\rho_i \sim 20$ –40. The ordering $\rho_i/L \ll 1$ assumed in the local analysis presented here is marginal at this location, in that global calculations have indicated that these parameters are near the point at which non-local effects are likely to quantitatively alter the results [14]. In the steep-gradient region nearer the separatrix, L/ρ_i is reduced further to ~ 5 , indicating that non-local effects are likely to be strong. With such large values of ρ_i/L , it is also possible that $\delta f/f$ is no longer small, and a full-f code should be used. Finally it should be noted that for edge parameters the saturated nonlinear modes may be quite different from the results of the linear simulations presented here [15, 16]. Nonetheless, these calculations provide a first qualitative look at the dominant instabilities and how they trend with quantities that are known to change with lithium; non-local, nonlinear simulations needed for quantitative transport predictions are a subject for future research. The consequences of the local approach are discussed in more detail in section 3.

For electron-scale instabilities (i.e. the ETG analysis presented here), however, $\rho_e/L \ll 1$ is well satisfied.

2. Survey of linear microstability properties without and with lithium

2.1. Simulation setup and example calculations

The linear microstability characteristics of the plasma edge profiles have been examined for the end-cases shown in figure 1 (without lithium and with maximum lithium deposition). Realistic magnetic geometries were used, based on kinetic equilibrium reconstructions including both the pedestal pressure profile and the bootstrap current, generated as part of edge peeling–ballooning analysis. To generate these equilibria, the measured pedestal profiles were fitted to a modified hyperbolic tangent form, and the bootstrap current calculated based on these profiles. The pressure and current were then used as constraints in an equilibrium reconstruction; the details of this process can be found in [5, 9]. The calculations are fully electromagnetic, including both δA_{\parallel} and δB_{\parallel} , and pitch-angle scattering collisions are included. In all calculations, the plasma profiles are taken from pedestal profile fits used in peeling–ballooning analysis [5], with three plasma species included: electrons, deuterons, and fully stripped carbon ions. Lithium is not directly included in the simulations, since its concentration in the plasma has been measured to be ~ 100 times less than that of carbon [3]. Extensive resolution scans have been performed to ensure convergence with respect to, e.g., number of poloidal grid points N_{θ} , poloidal extent of the grid, and time step dt , for the calculations presented here. These were performed at several radii—corresponding to the different mode types identified in figure 5—with values of $N_{\theta} = 72$, extent of three poloidal transits, and $dt = 0.01 a/c_s$ found to give good convergence for all cases.

Figure 3 shows example poloidal wavenumber spectra of the growth rate and real frequency at several radii in the two discharges examined. Using the GS2 initial value approach, this yields the growth rate of the most unstable mode, if multiple instabilities are present. The convention used here is that negative real frequency corresponds to the electron diamagnetic drift directions. Both discharges show unstable modes over a wide range of poloidal wavenumber, with very high $k_{\theta}\rho_s$ (up to ~ 150) instabilities present especially near the plasma edge.

Typical normalized eigenfunction profiles are shown in figure 4. These are from the highest growth rate modes at $k_{\theta}\rho_s \leq 1$ for the three radii shown in figure 3 for the case without lithium, and are chosen since they show a variety of parallel mode structures. At a radius of $\psi_N = 0.93$, the mode shows a tearing parity, with ϕ being odd around $\theta = 0$ and δA_{\parallel} even, as is typical of microtearing modes [17–19]. At $\psi_N = 0.95$, the mode shows a twisting parity, with ϕ even and δA_{\parallel} odd. The mode at $\psi_N = 0.97$ shows a similar parity. However, in this case the relative phase of the real and imaginary parts of δA_{\parallel} are different between the two cases, with the real and imaginary parts being out of phase at $\psi_N = 0.95$ and in-phase at 0.97. This is indicative of a change from a TEM-like mode at $\psi_N = 0.95$ to KBM-like at larger

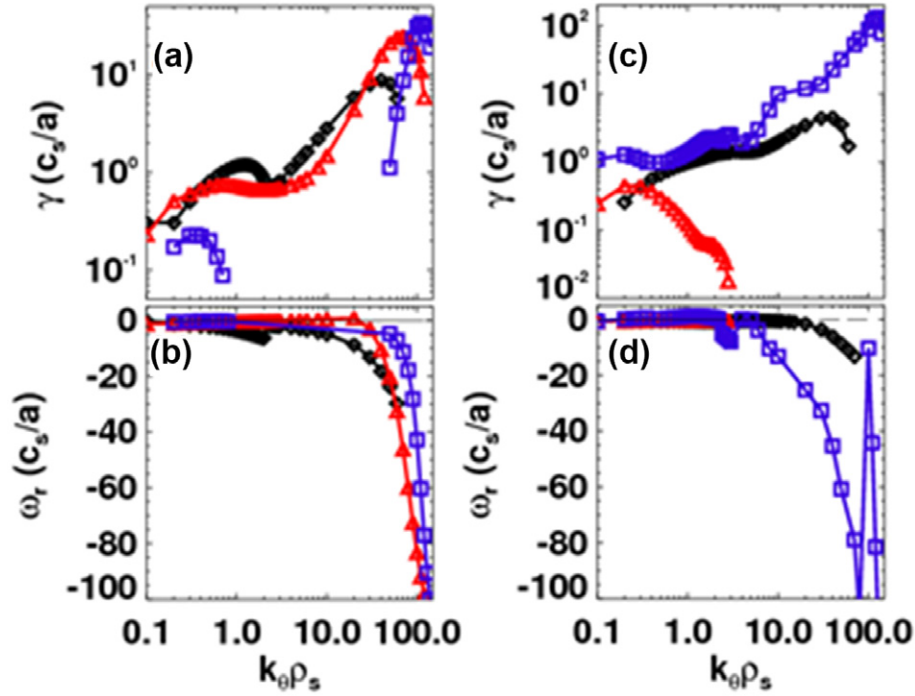


Figure 3. Spectra of growth rate and real frequency at (a), (b) $\psi_N = 0.93$ (black), 0.95 (red) and 0.97 (blue) without lithium, and (c), (d) $\psi_N = 0.88$ (black), 0.92 (red) and 0.97 (blue) with lithium.

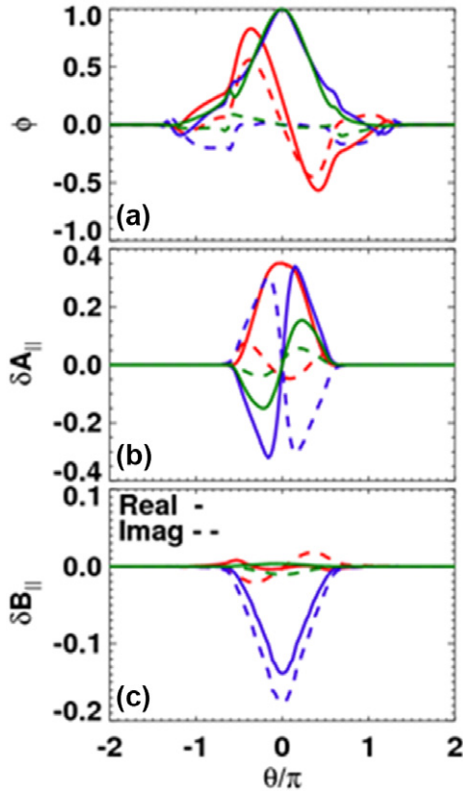


Figure 4. Eigenfunctions of the most unstable low- k mode for the discharge without lithium at $\psi_N = 0.93$ (red), 0.95 (blue) and 0.97 (green).

radius [20]. Furthermore, the strength of the compressional perturbations (δB_{\parallel}) is much larger in this case, approaching 20% of the electrostatic potential. These different mode

structures, along with the sign of the real frequency, allows one to distinguish the mode type (TEM/ITG versus KBM, TEM versus microtearing), and is often used in the present work to identify the dominant type of instability. This identification has been confirmed by thorough parameter scans to test for the expected scalings of the various modes (see section 2.3).

2.2. Dominant modes at $k_{\theta} \rho_s \leq 1$

For each plasma radius studied, linear growth rates are calculated over a range of $k_{\theta} \rho_s$. The results are summarized in figure 5, which shows radial profiles of the maximum growth rate from the $k_{\theta} \rho_s$ spectrum calculated at each radius. In this case, the $k_{\theta} \rho_s$ range is restricted to $k_{\theta} \rho_s \leq 1.0$ (electron-scale microstability is presented below). The type of mode is identified for different regions in the figure (ITG: ion temperature gradient; TEM: trapped electron; MT: microtearing; KBM: kinetic ballooning). The modes were identified based on parameter scans around the nominal operating point (described in section 2.3), the sign of the real frequency, and by the eigenfunction structure in the case of MT [21] and KBM [20]. Also shown is the $E \times B$ shearing rate [22] $\gamma_E = -(r/q)\partial/\partial r(E_r/RB_{\theta})$, calculated based on the measured C^{6+} toroidal velocity and pressure profiles (although poloidal rotation is not included here, analysis of other discharges suggests that it is a small contributor to the total radial electric field [23]).

For the no-lithium pedestal, four distinct regions can be identified. Beginning with the outermost, the region at the foot of the pedestal near the separatrix is unstable to KBM-like modes, with growth rates that are much larger than the shear rates. Within the pedestal, where the pressure gradient is large, TEM is dominant (more precisely, a hybrid TEM/KBM mode very sensitive to β_e [24]), with growth rates reduced

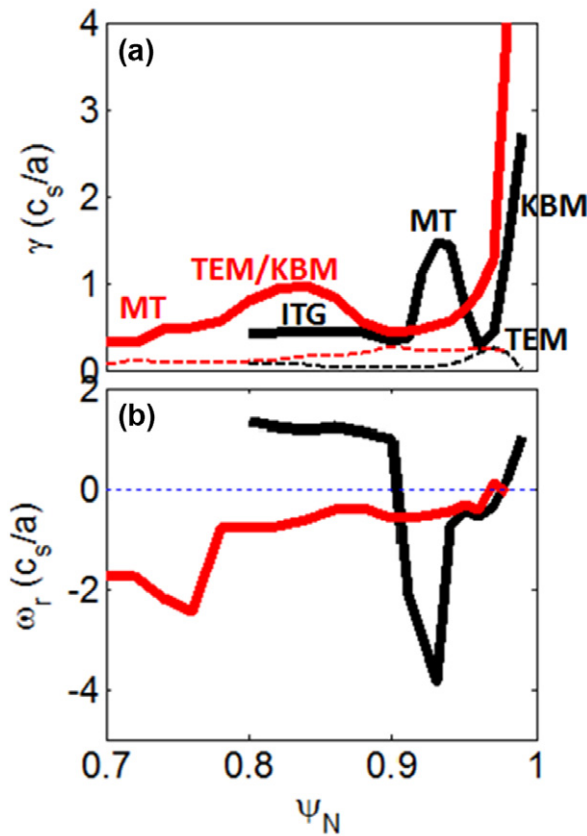


Figure 5. Profiles of (a) growth rate (solid) and $E \times B$ shear rate (dashed), and (b) real frequency of the most unstable mode with $k_{\theta}\rho_s \leq 1$ without (black) and with (red) lithium.

to within a factor of ~ 2 of the shear rate. At the pedestal top (near the inflection point in the n_e and T_e profiles), the dominant mode is MT, once more with growth rates much larger than the shear rate. Finally, inside the pedestal region (near the core), ITG is dominant. It should be noted that multiple modes may be present within the different regions that cannot be analysed with the initial value approach used here; an eigenvalue solver [20] would be required to discern the subdominant modes. With lithium, the radial structure of the growth rates is qualitatively similar, but with broader corresponding radial regions due to the overall widening of the pedestal. In this case, however, the dominant instability for all three edge-most regions is a TEM/KBM hybrid (see the discussion in sections 2.3 and 3), with MT appearing further in towards the core.

2.3. Scaling of dominant instabilities

The scaling of the dominant modes in several of the regions highlighted in section 2.1 with various parameters (gradient scale lengths, collisionality, etc) have been studied in order to determine the dominant mode type, as well as to help identify the mechanism behind the changes as lithium is applied. In doing these scans, care must be taken in how the magnetic geometry is handled. The nominal geometry is constructed from a numerical equilibrium constrained by measurements, which is consistent with the experimental kinetic profiles. From this equilibrium, the pressure gradient and magnetic

shear can be independently varied to produce neighbouring equilibria still locally satisfying the Grad–Shafranov equation [25, 26]. When varying parameters such as the density gradient, the pressure gradient of the kinetic profiles departs from the pressure gradient in the original equilibrium. Thus, one can either use the original geometry which has a (constant) pressure gradient that becomes inconsistent with the kinetic profiles as they are varied, or one can construct a new equilibrium at each point in the scan using a pressure gradient that it is consistent with the kinetic parameters as they are varied. While the latter approach is more physically relevant, the former is useful for identifying mode types based on their parameter dependencies. Increasing the pressure gradient in the geometry has a stabilizing effect on the magnetic drifts that tends to be quite strong in spherical torii [27], and so these two approaches can yield very different behaviours during parameter scans; both approaches are used here.

2.3.1. Scaling of pre-lithium pedestal-top microtearing. A clear difference between the microstability properties between the pre- and with-lithium cases is in the presence of strong MT modes in the region $\psi_N \sim 0.91$ – 0.94 ; this is the pedestal-top region without lithium. With lithium these modes are not present, and this region corresponds to the mid-pedestal region with strong gradients in n_e , T_e , and pressure. To understand the transition between the pre-lithium and with-lithium cases, parameter scans have been performed beginning with the pre-lithium values and scaling them towards those measured with lithium. Figure 6 shows the scaling of the $k_{\theta}\rho_s = 1.0$ growth rate for $\psi_N = 0.93$ in the discharge without lithium (at the pedestal-top where MT is dominant) with density gradient and with the electron–ion collision frequency. For each point in the density gradient scan, the pressure gradient of the local magnetic equilibrium has been adjusted to be consistent with the kinetic profiles according to $\partial\beta/\partial r = \beta_e \Sigma_s n_s T_s (a/Ln_s + a/LT_s)$ (see, e.g., [27]). The nominal experimental values are indicated by the vertical dashed lines. For this region, increasing the density gradient is stabilizing to the dominant MT instability (this is partially due to the stabilizing influence of the pressure gradient on the geometry [27]), allowing TEM/KBM hybrid mode to become dominant at higher density gradients, with much reduced growth rates at the $a/Ln_e \sim 10$ measured at the same radius in the case with lithium. Scans of the electron and ion temperature gradients show a much weaker dependence, so that the dependence on density gradient is dominant. It thus appears that, with ELMs avoided with lithium, the density and pressure gradient at the pedestal top increase and strongly stabilize the MT modes dominant there, allowing the pedestal to continue to grow inwards (this is a similar qualitative picture to that reported based on analysis of MAST plasmas [21]). At that radius, the MT mode depends weakly on collisionality, and is modestly stabilized with increasing ν_e (panel (c)); a similar dependence on collisionality has also been found for pedestal-top microtearing modes at MAST [28] and JET [29].

2.3.2. Scaling of mid-pedestal TEM/KBM mode. As described above, within the pedestal, where the pressure gradient is large, a hybrid TEM/KBM mode is dominant. This is present both without and with lithium, although the region

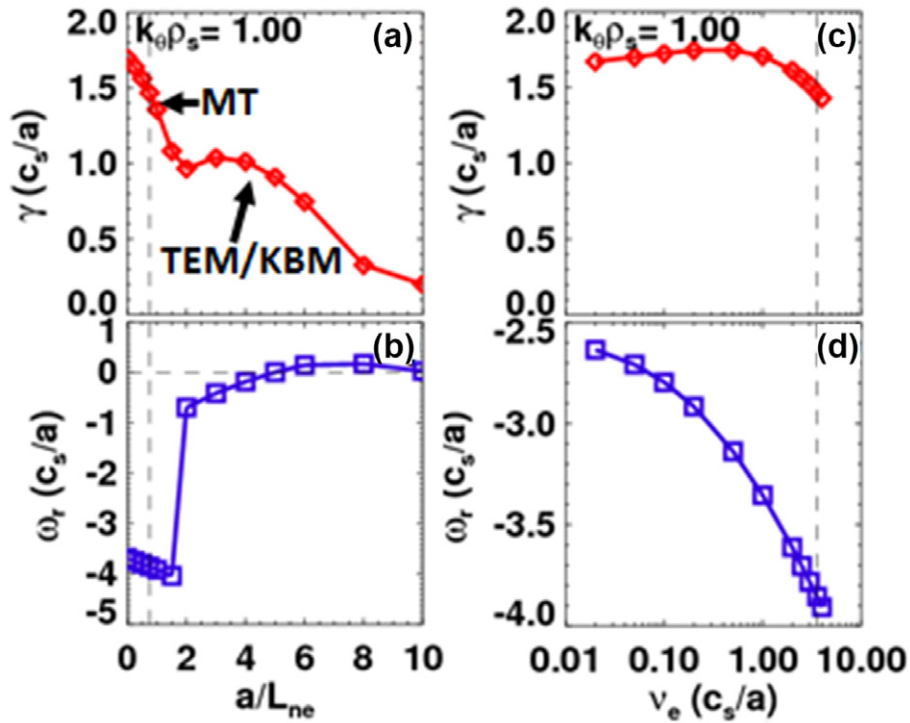


Figure 6. Scaling of growth rate and real frequency with (a), (b) density gradient and (c), (d) collisionality for $\psi_N = 0.93$ without lithium.

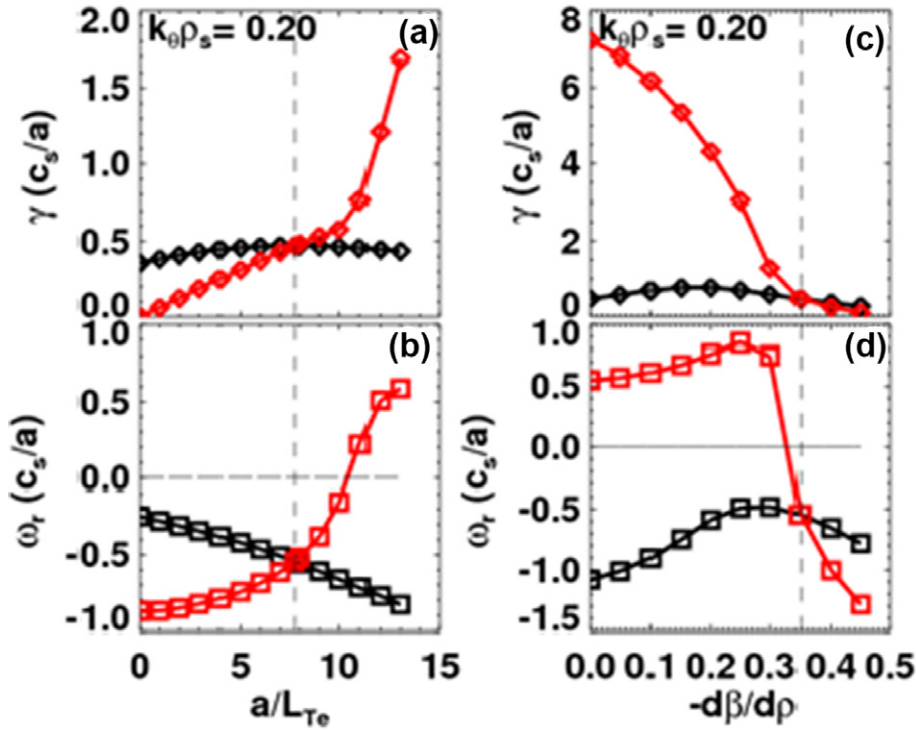


Figure 7. Scaling with (a), (b) electron temperature gradient and (c), (d) pressure gradient used in equilibrium for $\psi_N = 0.92$ with lithium. Parameters are scanned individually (red) or consistently between geometry and profiles (black).

where it is the most unstable mode varies between the two. The mode identification in this case has been made primarily on a set of parameter scans, which show features consistent with both the TEM and the KBM. Figure 7 shows the scaling with electron temperature gradient and with pressure gradient

of the dominant mode in the with-lithium case at a radius of $\psi_N = 0.92$ (in terms of relative position within the pedestal, this location is similar to the steep-gradient region at $\psi_N = 0.97$ without lithium). Increasing the T_e gradient is strongly destabilizing when scaled alone, consistent with TEM, and

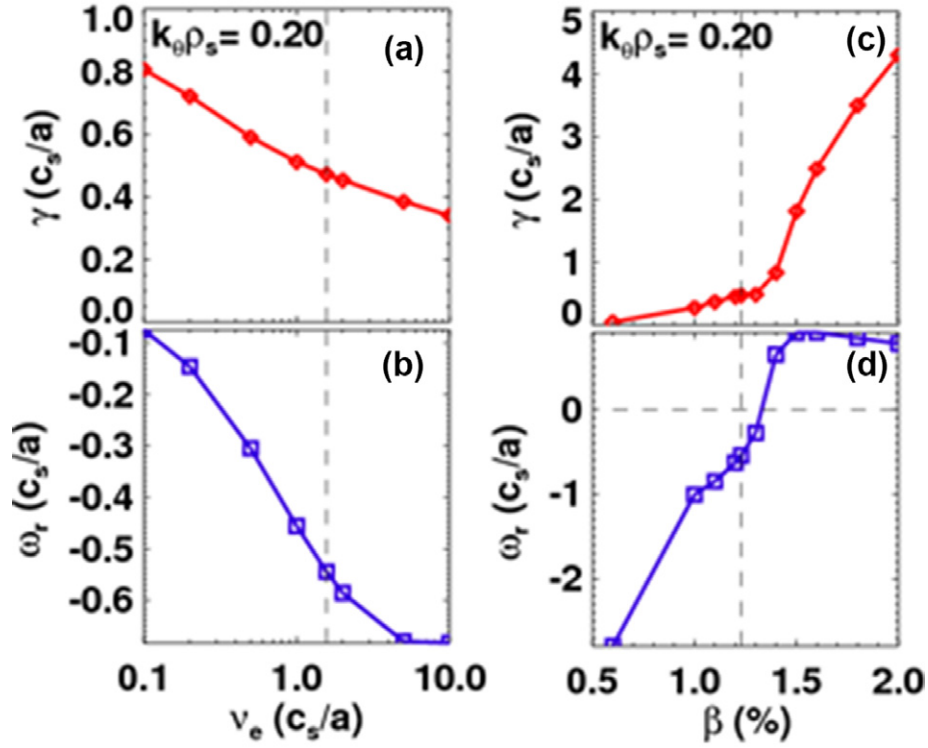


Figure 8. Scaling with (a), (b) collision frequency and (c), (d) β_e for $\psi_N = 0.92$ with lithium. Experimental parameters are indicated by vertical dashed lines.

shows a sharp up-turn at high gradient that is due to KBM onset (as evidenced by the real frequency changing sign (panel (b)) as well as a change in the eigenfunction structure). When $\partial\beta/\partial r$ of the geometry is scaled consistently with the T_e gradient the destabilization is much weaker and the transition to KBM does not occur. The stabilizing influence of $\partial\beta/\partial r$ in the equilibrium is seen by scaling it alone (panel (c), red curves). When β_e of the profiles is scaled consistently with the $\partial\beta/\partial r$ (panel (c), black curves), the dependence is again much weaker. Even with β_e scaled consistently, however, increasing pressure gradient remains stabilizing at the experimental parameters. This is in contrast with the sharp increase of growth rates that is observed in KBM calculations in conventional geometries [30].

Figure 8 shows the scaling with collisionality and with β_e ; here β_e is scaled alone without scaling $\partial\beta/\partial r$ to be consistent, since the consistent case is shown in figure 7. The growth rate decreases as collisionality is increased, which like the a/L_{T_e} dependence is consistent with the expected scaling for TEM [31]. KBM onset is clear in the β_e scan, with sharply increasing growth rates and a transition to an ion-direction real frequency. However, even below this threshold where the TEM-like mode is dominant, increasing β_e is destabilizing, in contrast to the weak to non-existent β_e dependence typically observed for TEM [20]. Since the mode has features consistent with both TEM and KBM, and given that the real frequency varies smoothly from negative to positive as either a/L_{T_e} or β_e are increased (rather than showing a discrete jump in frequency), this is identified as a TEM/KBM hybrid. This is similar to ITG-KBM modes identified in [20], and modes with similar behaviour have also been identified in core NSTX calculations [24].

2.4. ETG stability

It has been suggested that ETG modes could play a role in the transition from no-lithium to strong lithium deposition [7], in particular in the region outside $\psi_N \sim 0.95$ where the T_e profile is observed to be rather stiff. To explore this possibility, the stability of electron-scale modes has been investigated in more detail. As shown in figure 3, high- $k_\theta \rho_s$ ETG modes are often calculated to be unstable in the edge region of interest for both the without- and with-lithium cases. Figure 9 shows the radial profile of the maximum growth rate for $k_\theta \rho_s \geq 10.0$ for the without- (black) and with-lithium (red) cases. Both discharges show a region of ETG instability near the plasma edge, in the region where the T_e profile is stiff. However, the growth rates increase substantially with lithium, with normalized values increasing by a factor of ~ 4 . This is due to a significant reduction in the critical ∇T_e for ETG onset with lithium (panel (b)). Further, the growth rates increase more strongly with increasing T_e gradient with lithium (panel (b)), indicating that transport due to ETG is stiffer in this case.

The change in ETG stability is due to the change in profiles in this region that occur with lithium: ∇T_e is relatively unchanged while ∇n_e is reduced a factor of ~ 2 , so that η_e is significantly higher, leading to stronger ETG instability. The role of ∇n_e [32] has been confirmed by calculations with the ∇n_e interchanged between the two shots (i.e. the without-lithium case run using the with-lithium ∇n_e , and vice versa); the results are shown as the dashed curves in panel (b). The change in ETG onset and stiffness suggest that transport due to this mode would be a stronger contributor with lithium. A possible explanation for the profile changes that occur due to lithium is that without lithium, ETG transport

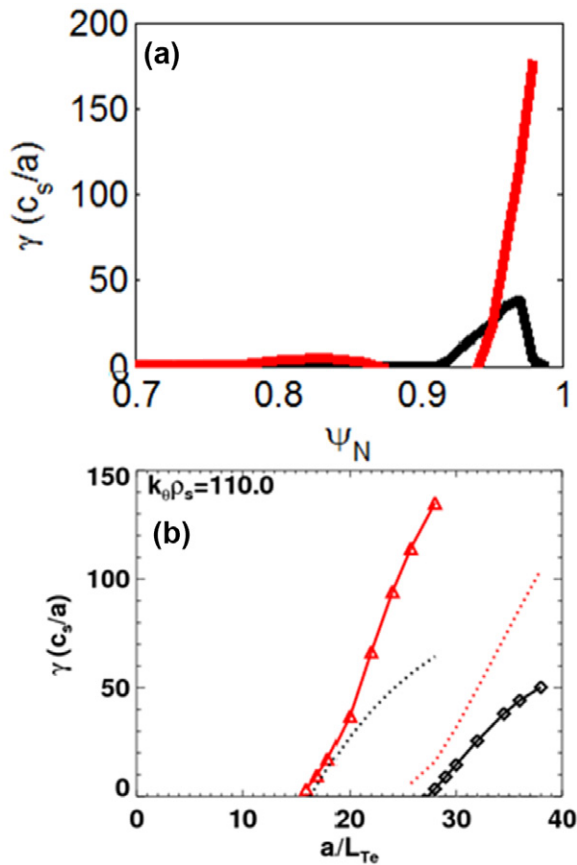


Figure 9. (a) profile of growth rate of the most unstable mode with $k_\theta \rho_s \geq 10$ and (b) dependence of growth rate on electron temperature gradient without (black) and with (red) lithium, and with density gradient interchanged between the two cases (dotted).

may be negligible, and become stronger as lithium is added. This would prevent ∇T_e from increasing even though n_e is lower, and so the pressure gradient would be reduced, resulting in a lower bootstrap current, which has been shown to play a central role in explaining the stabilization of ELMs observed with lithium [5]. For this picture to be valid, however, requires that the heat fluxes due to ETG modes be large enough to explain the experimental profile changes. Performing nonlinear simulations of the ETG transport to test this hypothesis quantitatively will be a focus of future research.

3. Ballooning stability

A recent model for the pedestal height and width has been proposed (the EPED model [8]), in which KBMs are assumed to limit the local pedestal pressure gradient between ELMs. KBM onset in this model is assumed to correspond with ideal infinite- n ballooning mode instability, which can be rapidly calculated. EPED has been tested against a large database of measured pedestal parameters, and has successfully predicted the height and width over a wide range of experiments [33, 34]. Given the success of EPED, the KBM is considered a leading candidate for dominating pedestal transport. In light of this, the ballooning stability of NSTX discharges has been studied

in detail. Calculations have been performed of ideal, infinite- n ballooning stability, which KBM is expected to follow for the most part, along with gyrokinetic calculations of KBM stability.

3.1. Ideal ballooning calculations

The infinite- n , ideal ballooning stability [35] has been calculated for the without- and with-lithium cases described above, with the results summarized in figure 10. In this figure, the ‘first stability’ curve is the value of the pressure gradient at which the ballooning stability boundary is reached (starting from no gradient). The plasma is unstable to ballooning modes between this and the ‘second-stability’ boundary, above which the modes are stable [36]. At some radii instability is never reached; this is due to the magnetic shear $s = (r/q)(dq/dr)$ in the experimental reconstruction being lower than the minimum value at which ballooning goes unstable (see, e.g., figure 11). The shear in the equilibrium as well as the shear at the minimum-shear point on the ballooning boundary is shown in panels (b) and (d).

The calculations show that only for the very edge of the plasma, $\psi_N \geq 0.98$, is the experimental pressure gradient near the first stability boundary. Inside this radius, ballooning modes are stable for all pressure gradients at the experimental level of shear, indicating that second-stability effects are strong. Thus, the ideal calculations indicate that ballooning modes can’t limit pressure gradient except for very near the separatrix. However, this result is due to the low value of the magnetic shear within the pedestal, which is subject to substantial uncertainty. While difficult to precisely quantify since it not directly measured, the uncertainty in the edge current in these discharges has been previously estimated to be $\sim 30\%$ [9] (with a similar error in the shear), which is comparable to the difference between the experimental value shown in figure 10 and the shear at the minimum- s point. Recent work has uncovered further possible uncertainties in the edge current, including the model used to calculate it [37], which has been shown to underestimate the current in spherical tokamaks [38], as well as systematic over- or under-estimations of the local gradients within the pedestal imposed by the fitting form used [39]. Thus, while local ballooning analysis suggests most of the pedestal is ballooning stable, more of the pedestal would become unstable if the magnetic shear has been underestimated by $\sim 30\%$. On the other hand, if the bootstrap current is larger (as suggested by [38]), the shear would be further reduced, making ballooning modes even more stable. While the stability to ballooning modes appears to be inconsistent with the EPED model [8], which uses a ‘ballooning critical pedestal’ constraint on the pressure gradient, taken to be the pressure profile at which half of the pedestal is ballooning unstable [33], we note that EPED further assumes that KBMs do not exhibit second stability. Better quantifying the various sources of uncertainty in the edge current profile and analysing their impact on ideal ballooning will be a focus of future research.

3.2. Calculations of KBM stability

The stability of KBMs has been calculated using GS2. To explore stability space, calculations are performed over a range

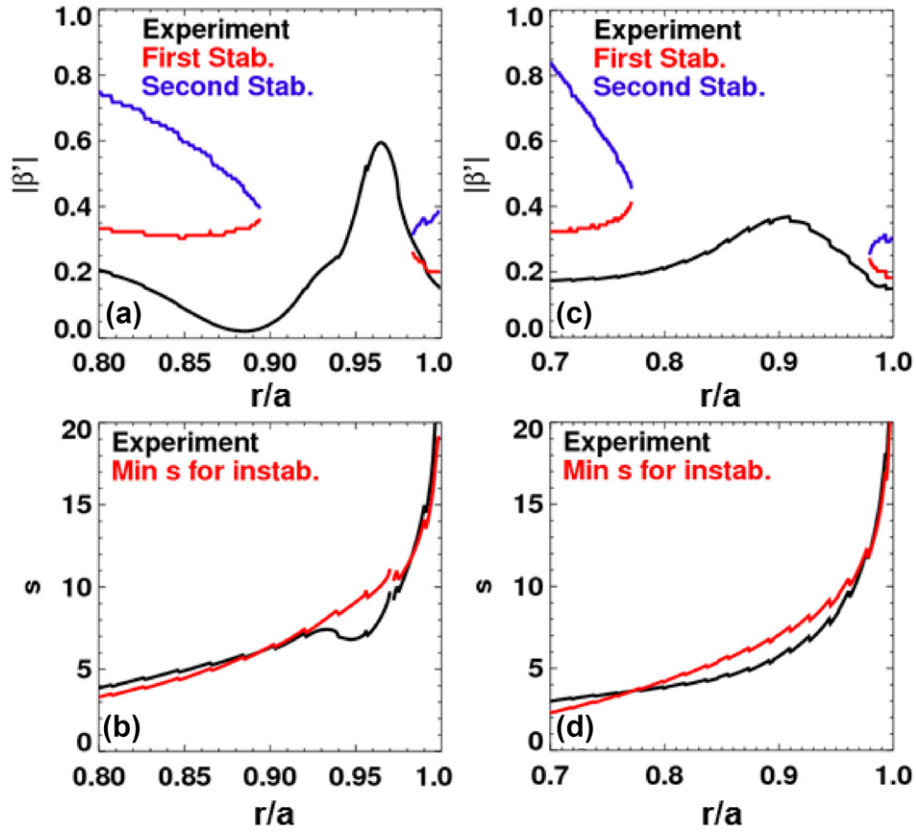


Figure 10. Profiles of experimental pressure gradient and ballooning boundaries (a) without and (c) with lithium; experimental shear and minimum shear for ballooning instability (b) without and (d) with lithium.

of magnetic shear and pressure gradient, for a fixed radius and $k_\theta \rho_s$. In this scan, the pressure gradient in the equilibrium and β_e in the profiles are scaled together consistently. Figure 11 shows an example of the calculated growth rates and real frequency in this 2D space, for the with-lithium case at a radius of $\psi_N = 0.94$. The ideal boundary is also shown.

The growth rate contours largely follow the ideal ballooning boundary (red curves), with the maximum growth rate occurring close to the first stability boundary and rapidly falling off as the pressure gradient is increased towards second-stability region for ideal ballooning that exists at high pressure gradient and at low shear. The real frequency closely tracks the ideal boundary, with frequencies changing from negative to positive near the boundary. The relative sign of the real and imaginary parts of the δA_\parallel eigenfunctions is shown in panel (c)), with positive values indicating the in-phase parity that typically occurs for KBM instabilities (see section 2.1). The region identified as having KBM-like eigenfunctions corresponds closely with the ideally unstable region. The region outside the ideal stability boundary is identified as TEM, based on the eigenfunction phasing and the negative real frequencies. Thus, in this case the KBM-unstable region corresponds very closely with the ideal calculations (as has also been observed in MAST pedestal simulations [40]). While kinetic effects are expected to expand the KBM-unstable region somewhat [30], since the initial value approach used here only yields the most unstable mode, it may be that KBM is unstable outside this

region but subdominant to TEM. As noted in section 2.3, increasing pressure gradient is stabilizing at experimental parameters. Similar results are obtained for the case without lithium, with KBM stability following the ideal boundary, and TEM smoothly transitioning to KBM as parameters are varied.

The smooth variation of the real frequency with both the shear and pressure gradient again suggest that this is a hybrid TEM-KBM mode [24] rather than two discrete branches that are competing for dominance. This hybrid mode is not present in calculations where compressional perturbations are not included, requiring δB_\parallel be included in the calculations to be unstable. As figure 12 shows, if compressional perturbations are neglected, the KBM branch of the mode is stable, and a negative real frequency mode remains dominant as the pressure gradient is increased through the ideally ballooning-unstable region. (Note that in the case shown in figure 12, the magnetic shear has been increased to $s = 15$ so that the ideal ballooning instability is encountered during the pressure gradient scan). This behaviour with respect to δB_\parallel has also been observed in core NSTX calculations using the GYRO code that also show a TEM/KBM mode [24], and the need for including δB_\parallel for KBM-like modes is discussed in detail in [41].

These linear gyrokinetic calculations, along with the ideal calculations, do not support the notion that KBMs limit the pedestal pressure gradient except near the very edge. Ballooning modes are calculated to be in the second-stable regime for most of the pedestal, and although as discussed

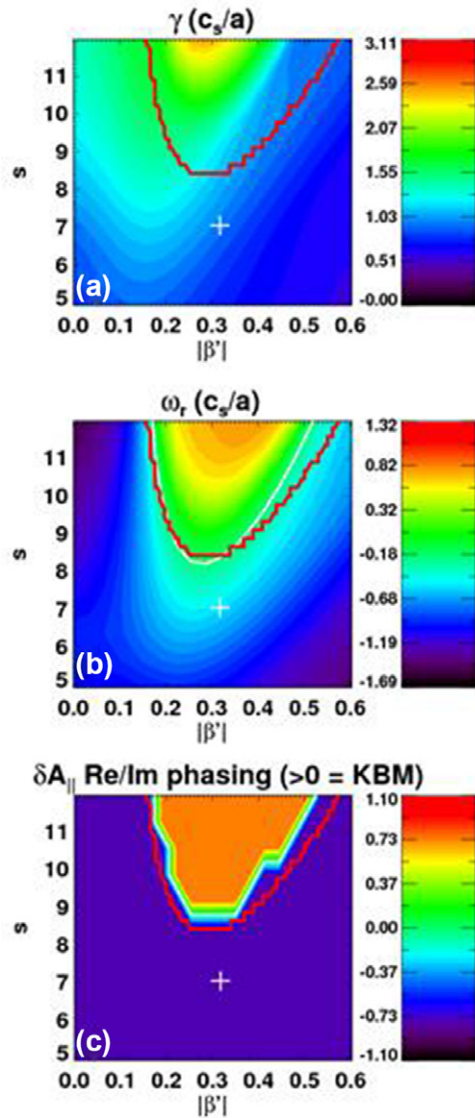


Figure 11. Contours of (a) growth rate and (b) real frequency and (c) relative sign of the real and imaginary parts of the $\delta A_{||}$ eigenfunctions versus pressure gradient and shear for $\psi_N = 0.94$ with lithium. Crosses indicate experimental values, and red curves indicate ideal ballooning stability boundary.

above this may not be realistic given the uncertainty in the magnetic shear, at the experimental value of the pressure gradient the growth rates are predicted to decrease with further increases to the pressure gradient for all values of shear shown (i.e. even within the ideally unstable region where KBMs are predicted). This is in conflict with the usual picture of KBMs as stiffly limiting the pressure gradient [33]. However, it should be noted that these calculations are local and do not include profile effects. It is possible that non-local effects in the gyrokinetic calculations would remove the second-stable region—similar to the elimination of second stability often observed in finite- n MHD calculations compared to infinite- n [42]—resulting in KBMs being unstable at the experimental pressure gradient and shear. In the future, global gyrokinetic calculations will be used to study this effect (the need for such calculations is also clear from the ordering parameters discussed above).

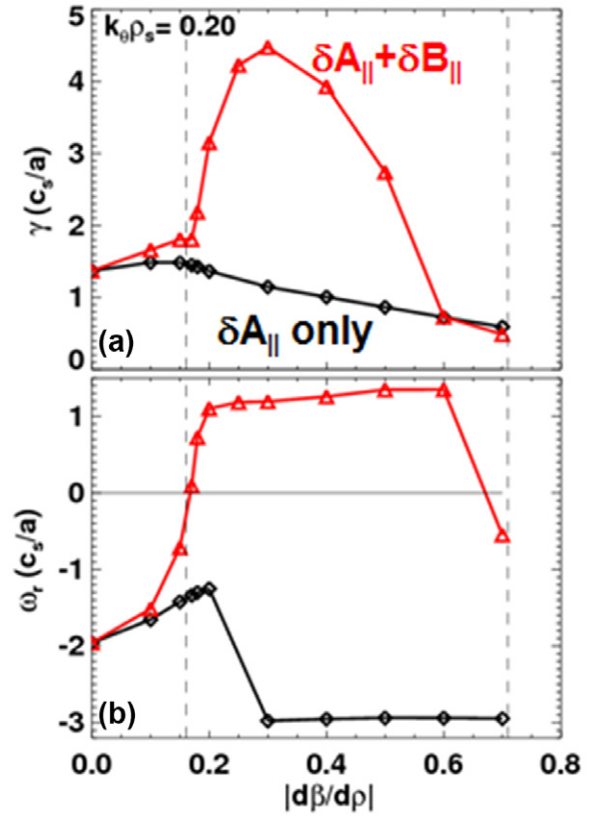


Figure 12. Scaling of (a) growth rate and (b) real frequency with pressure gradient for $\psi_N = 0.94$ with lithium (but with shear set to $s = 15$), with (red) and without (black) $\delta B_{||}$. Ideal first- and second-stability boundaries are indicated by dashed vertical lines.

4. Summary and conclusions

A survey of the linear microstability properties of the NSTX edge plasma without and with lithium-coated PFCs has illuminated several features that could contribute to the observed ELM elimination and improved energy confinement. At the pedestal top, where 2D modelling indicates a reduction in transport coefficients as lithium is applied to the PFCs, microtearing appears to be the dominant instability without lithium. These modes are stabilized by increasing density gradient, and weakly destabilized by collisionality; similar dependences of pedestal-top microtearing instabilities have also been found in [21, 28, 29]. With lithium, the density gradient is strongly increased at the same radius, so that the microtearing modes are stabilized and a TEM/KBM mode becomes dominant with a substantially reduced growth rate. While the detailed cause of the change in density profile with lithium is unclear (beyond the strong reduction in recycling with lithium), the decrease in energy transport at the pedestal top and widening of the steep-gradient region observed with lithium is consistent with the stabilization of microtearing modes by the density gradient as the pedestal grows inwards. Quantifying the particle and energy fluxes (both through quasilinear estimates and nonlinear calculations) will be a focus of future efforts to better understand the pedestal-top changes to the temperature and density profiles.

While the decrease in pedestal-top transport appears to be due to the stabilization of microtearing modes, an

outstanding issue is how the transport is changed within the pedestal such that ELMs are eliminated and the pedestal is free to grow. As described in section 1.1, the electron temperature profile is rather stiff near the separatrix, with little change in T_e measured outside $\psi_N \sim 0.95$ regardless of how much lithium is applied. This resiliency is critical to the ELM behaviour, since the stiffness of the T_e gradient results in reduced pressure gradient as the density is reduced with lithium, resulting in a lower bootstrap current and less drive for peeling–ballooning modes. ETG modes at very high $k_\theta \rho_s$ have been identified as one possible mechanism for limiting the near-separatrix T_e gradient. Linearly, these are calculated to be much more unstable with lithium and hence may provide an additional transport channel that keeps the pressure (and bootstrap current) low near the separatrix. However, the transport due to these modes must be calculated to test if they can provide an experimentally relevant amount of heat flux. As part of future research, the role of high- k modes will be explored by performing nonlinear simulations in order to quantify how much transport results from ETG turbulence.

The role of KBMs in limiting the pedestal pressure gradient has also been examined, motivated by the success of the EPED model. Ideal, infinite- n calculations show that the pedestal is second-stable to ballooning modes, although this may be within the uncertainty in the edge current profile. Gyrokinetic calculations show that, at high density and pressure gradients, either in the pedestal in the without-lithium case or in the broader region observed to have high gradients with lithium, a mode identified as a hybrid TEM/KBM is dominant, with features consistent with both TEM and KBM. The transition from dominantly TEM-like to KBM-like has been shown to follow closely the ideal ballooning boundary, based on the real frequency and eigenfunction structure. At the experimental parameters this mode is TEM-like, consistent with KBMs being second stable, and perhaps more importantly shows a growth rate that decreases with increasing pressure gradient (this is true over a broad range of shear). While the local calculations presented here therefore indicate that KBM onset does not appear to limit the pedestal pressure gradient, it should be emphasized that non-local effects are expected to be strong within the pedestal and are not captured in this analysis. Future research will employ global gyrokinetic calculations [14] that are necessary to more quantitatively analyse the pedestal region.

Acknowledgments

Research sponsored by the US Department of Energy under contracts DE-AC05-00OR22725, DE-FG02-99ER54527,

DE-AC02-09CH11466, DE-FC02-04ER54698 and DE-AC52-07NA27344.

References

- [1] Maingi R. et al 2011 *Phys. Rev. Lett.* **107** 145004
- [2] Maingi R. et al 2012 *Nucl. Fusion* **52** 083001
- [3] Bell M.G. et al 2009 *Plasma Phys. Control. Fusion* **51** 124054
- [4] Mansfield D.K. et al 2009 *J. Nucl. Mater.* **390–391** 764
- [5] Maingi R. et al 2009 *Phys. Rev. Lett.* **103** 075001
- [6] Schneider R. et al 2006 *Contrib. Plasma Phys.* **46** 3
- [7] Canik J.M. et al 2011 *J. Nucl. Mater.* **415** S409
- [8] Canik J.M. et al 2011 *Phys. Plasmas* **18** 056118
- [9] Boyle D.P. et al 2011 *Plasma Phys. Control. Fusion* **53** 10501
- [10] Kaye S.M. et al 2013 *Nucl. Fusion* **53** 063005
- [11] Snyder P.B. et al 2002 *Phys. Plasmas* **9** 2037
- [12] Kotschenreuther M. et al 1995 *Comput. Phys. Commun.* **88** 128
- [13] Snyder P.B. et al 2009 *Phys. Plasmas* **16** 056118
- [14] Görler T. et al 2011 *Phys. Plasmas* **18** 056103
- [15] Scott B.D. 2005 *Phys. Plasma* **12** 062314
- [16] Scott B.D. 2010 *Contrib. Plasma Phys.* **50** 228
- [17] Applegate D.J. et al 2004 *Phys. Plasmas* **11** 5085
- [18] Applegate D.J. et al 2007 *Plasma Phys. Control. Fusion* **49** 1113
- [19] Guttenfelder W. et al 2012 *Phys. Plasmas* **19** 022506
- [20] Belli E.A. and Candy J. 2010 *Phys. Plasmas* **17** 112314
- [21] Dickinson D. et al 2012 *Phys. Rev. Lett.* **108** 135002
- [22] Waltz R.E. and Miller R.L. 1999 *Phys. Plasmas* **6** 4265
- [23] Maingi R. et al 2010 *Phys. Rev. Lett.* **105** 135004
- [24] Guttenfelder W. et al 2013 *Nucl. Fusion* **53** 093022
- [25] Greene J.M. and Change M.S. 2001 *Nucl. Fusion* **41** 1601
- [26] Bishop C.M. et al 1984 *Nucl. Fusion* **24** 1579
- [27] Bourdelle C. et al 2003 *Phys. Plasmas* **10** 2881
- [28] Dickinson D. et al 2013 *Plasma Phys. Control. Fusion* **55** 074006
- [29] Saarelma S. et al 2013 MHD and Gyro-kinetic stability of JET pedestals, (arXiv:org/abs/1301.2919)
- [30] Snyder P.B. and Hammitt G.W. 2001 *Phys. Plasmas* **8** 744
- [31] Peeters A.G. et al 2005 *Phys. Plasmas* **12** 022505
- [32] Ren Y. et al 2012 *Phys. Plasmas* **19** 056125
- [33] Snyder P.B. et al 2011 *Nucl. Fusion* **51** 103016
- [34] Snyder P.B. et al 2012 *Phys. Plasmas* **19** 056115
- [35] Connor J.W., Hastie R.J. and Taylor J.B. 1979 *Proc. R. Soc. Lond. A* **365** 1
- [36] Greene J.M. and Chance M.S. 1981 *Nucl. Fusion* **31** 453
- [37] Sauter O. et al 1999 *Phys. Plasmas* **6** 2834
- [38] Koh S. et al 2012 *Phys. Plasmas* **19** 07205
- [39] Schneider P.A. et al 2012 *Phys. Plasmas Control. Fusion* **54** 105009
- [40] Dickinson D. et al 2011 *Plasma Phys. Control. Fusion* **53** 115010
- [41] Joiner N., Hirose A. and Dorland W. 2010 *Phys. Plasmas* **17** 072104
- [42] Snyder P.B. and Wilson H.R. 2003 *Plasma Phys. Control. Fusion* **45** 1671